ACS APPLIED MATERIALS & INTERFACES

RESEARCH ARTICLE

www.acsami.org

Controlled Growth of Self-Organized Hexagonal Arrays of Metallic Nanorods Using Template-Assisted Glancing Angle Deposition for Superhydrophobic Applications

Ganesh K Kannarpady,*[,†] Khedir R Khedir,[†] Hidetaka Ishihara,[†] Justin Woo,[†] Olumide D Oshin,[†] Steve Trigwell,[‡] Charles Ryerson,[§] and Alexandru S. Biris*[,†]

[†]Nanotechnology Center, University of Arkansas at Little Rock, 2801 South University Avenue, Little Rock, Arkansas 72204

[‡]Applied Science and Technology, ASRC Aerospace, ASRC-24 Kennedy Space Center, Orlando, Florida 32899

[§]Terrestrial and Cryospheric Sciences Branch, Cold Regions Research & Engineering Laboratory, Engineer Research and Development, Center U.S. Army Corps of Engineers, Hanover, New Hampshire 03755-1290

ABSTRACT: The fabrication of controlled, self-organized, highly ordered tungsten and aluminum nanorods was accomplished via the aluminum lattice template-assisted glancing angle sputtering technique. The typical growth mechanism of traditional glancing angle deposition technique was biased by self-organized aluminum lattice seeds resulting in superior quality nanorods in terms of size control, distribution, and long range order. The morphology, size, and distribution of the nanorods were highly controlled by the characteristics of the template seeds indicating the ability to obtain metallic nanorods with tunable distributions and morphologies that can be grown to suit a particular application. Water wettability of hexagonally arranged tungsten and aluminum nanorods was studied after modifying their surface with 5 nm of Teflon AF 2400, as an example, to exhibit the significance of such a controlled growth of metallic nanorods. This facile and scalable approach to generate nano seeds to guide GLAD, with nano seeds fabricated by anodic oxidization of aluminum followed by chemical etching, for the growth of highly ordered nanorods could have significant impact in a wide range of applications such as anti-icing coating, sensors, super capacitors, and solar cells.

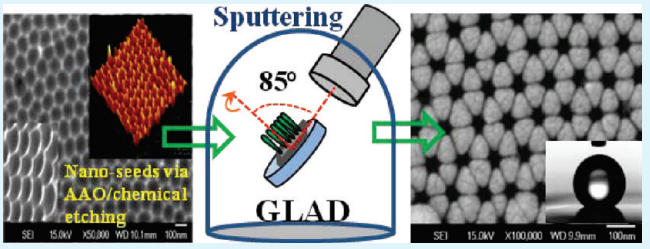

KEYWORDS: Metallic nanorods, GLAD deposition, Template assisted growth, Hexagonal self-organization, superhydrophobicity

1. INTRODUCTION

Self-organized and highly ordered nanostructures have great potential in a wide range of applications such as sensors,[1−4] capacitors,[5] and solar cells. Several methods have been employed to generate nanorods/nanowires such as chemical vapor deposition, physical vapor deposition, electrodeposition, etc.[6−9] Most of these techniques make use of a prepatterned template to define and control the size and distribution of the nanostructures.[10−12] This process can be quite complicated because the most commonly used methods for template generation are UV-lithography,[13,14] e-beam lithography,[15,16] and hot embossing,[17,18] which are time-consuming and difficult to scale up for large devices. On the other hand, the glancing angle deposition (GLAD) technique has gained a lot of interest for the last decade for the fabrication of a wide variety of nanostructural materials.[19−21] The main advantage of GLAD is that the generation of nanostructures is relatively easy, fast, and straightforward, with the nanomaterials' growth being achieved through controlled self-assembly. All of these practical considerations make this technique highly versatile, less hazardous in terms of chemical safety, and more efficient in terms of throughput. A wide variety of nanostructures—nanorods, nano wires, nano springs—can be generated easily by simply controlling the substrate tilt and rotation.[8,9] Although continuous progress is being reported[22] in various areas of GLAD technology, some of its major drawbacks concern the exact and precise control of the size and diameter distribution of the resulting nanostructures. The growth evolution of the GLAD-generated nanostructures is largely thickness-dependent and is characterized by diameter broadening, with random distributions—characteristics that collectively make this deposition method less attractive for applications that require periodic nanostructures with a long range order and controlled morphologies.

The traditional fabrication of metallic nanorods using conventional GLAD can be significantly altered and improved by using a pre-patterned substrate. In the pre-patterning process, seeds of controlled sizes and distribution are first fabricated over the substrate surface and then used during GLAD deposition for biased shadowing and improved control over the nanostructures' growth characteristics. This approach leads to a controlled condensation of the atoms deposited onto the seeds, which in turn results in highly ordered nanostructures. Various seed geometries and sizes have been obtained over various substrate materials.[23,24]

Received: February 28, 2011
Accepted: June 6, 2011
Published: June 06, 2011

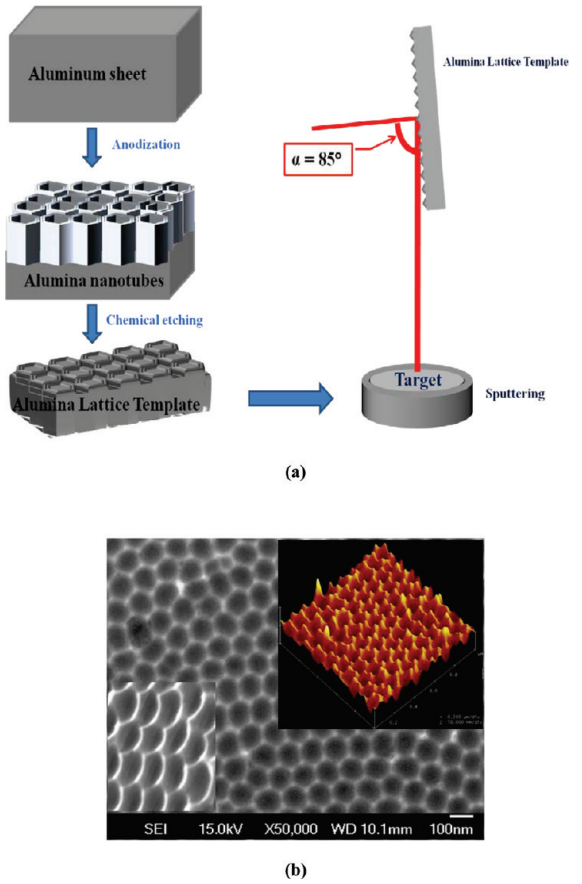

Figure 1. (a) Schematic overview of ALT-assisted GLAD growth of nanorods, (b) SEM image of aluminum lattice template. Top right inset is AFM image and bottom left inset is cross-sectional SEM.

The growth of nanostructures using GLAD on pre-patterned substrates was first carried out by Malac et al.[25] in 1999. This team generated highly ordered Ti and Co pillars on the pre-patterned substrate which was fabricated by e-beam lithography. Their work was followed by many other researchers who used various techniques to generate pre-patterned seeds: Dick et al.[26] used embossing; Ye et al.[27] used optical lithography; Jensen et al.[28] used laser-direct write lithography; Kesapragada et al.;[29] Zhao et al.[30] self-assembled colloids; and Zhou et al.[31] used self-assembled nanosphere lithography. However, most of these techniques for generating pre-patterned seeds suffer from their complexity, considerably low throughput, and limited scalability.[32,33] Although nanosphere lithography has made some remarkable progress recently in terms of scalability,[34,35] the development of a simple and easily scalable technique to pattern seeds is still required to make the seed-assisted GLAD technique more efficient and effective with applications in large scale industrial processes. We propose that one such technique for the growth of seeds could be the anodic oxidation of aluminum, which is a high throughput technique that could be applied to large scale surfaces. Electrochemical oxidation of aluminum yields alumina hexagonal nanotubes, as previously shown.[36] The diameter of the nanotubes (20 to 400 nm)[37] depends on the electrochemical anodization conditions which are easily controlled: temperature, voltage, and the chemicals used during the anodization process. The subsequent controlled chemical etching of alumina results in hexagonal lattice seeds of desired heights. The major goal of this report is to show that the use of such seeds to bias the ballistic shadowing process during the GLAD deposition is responsible for the growth of metallic nanorods with highly controllable arrangements and morphologies, which can be further used for supehydrophobic and ice-phobic coatings.

As previously shown, the overall surface roughness is an important factor in designing superhydrophobic surfaces with low adhesion for water. The development of sustainable and reliable technologies for the reduction of ice adhesion has been a great challenge, especially in very demanding aerospace applications. Although the superhydrophobic nature can be obtained on a microtextured rough surface, the use of nanotextured rough morphologies can be more efficient in avoiding the condensation of water vapors between nanogaps during dew conditions.[38] The condensation of tiny molecules of water in between the gap of nanorods can replace the air trapped; hence, the superhydrophobic nature can be significantly reduced. Thus, the growth of nano-textured rough surfaces is more desirable for an efficient superhydrophobic coating with low ice adhesion. Although rough metallic surfaces can be generated by many techniques, such as chemical etching and plasma etching, the GLAD technique has been gaining importance, recently, as a prominent technique to generate rough surfaces of various materials for water wetting applications. Fan et al.[39] fabricated vertically aligned nanorod arrays of Si using GLAD. They studied water wetting properties of Si nanorod arrays, after treating the surface with HF (Hydroflouric Acid), as a function of film thickness. Further, Fan and Zhao[40] studied the mechanism of water spreading on Si nanorod array surface generated by GLAD. The same research group recently reported a study of nanocarpet induced superhydrophobicity[41] on Si nanorod arrays generated by GLAD at different tilting angles in the range of 84−88°. Ye and Lu[42] have studied the effect of the shape and size of nanotips on the hydrophilicity of metallic surfaces. Also recently, we have tailored tungsten nanorod surfaces generated by GLAD to obtain tunable water repelling properties with contact angles in the range 122−160°.[43] Although these works show some degree of control over the water wetting properties of GLAD-generated nanostructures, further research and development is still required to generate highly ordered nanostructures over a large area to realize the potential of such nanostructures for various water spreading/repelling applications.

Here, we report a facile approach to fabricate highly ordered self-organized metallic nanorods. The nanoscale seeds for the growth of the nanorods were generated by anodic oxidization of aluminum followed by chemical etching. The glancing angle RF magnetron sputtering technique was used to deposit both tungsten and aluminum over the aluminum lattice seeds. The growth mechanism of the two metals used as models—one with a high melting point (tungsten) and the other with a low melting point (aluminum)—over the aluminum lattice seeds was studied in order to understand the effects of ballistic shadowing during the growth process. Finally, the nature of water interaction with the tungsten and aluminum nanorods' surfaces generated by this method was investigated by studying the static contact angle after the deposition of a thin (5 nm) layer of Teflon AF 2400 (TAF) over the top portions of the nanorods. We have proved that the surface energy of the resulting surfaces can be tuned to show superhydrophobic behavior with potential applications in aeronautics, ice mitigation, energy generation devices, and distribution.

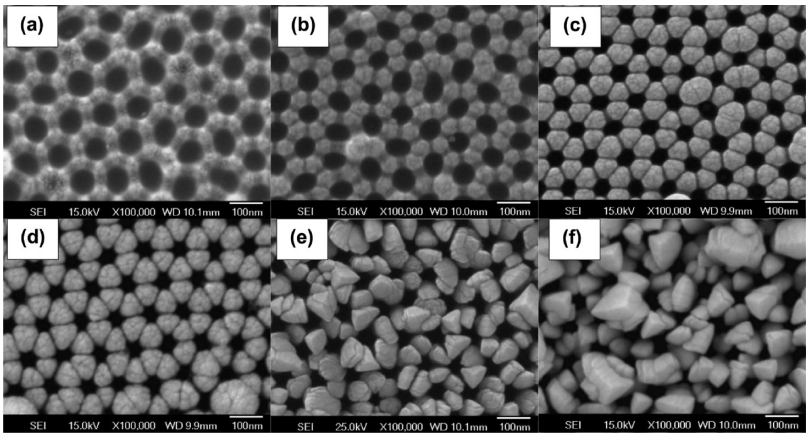

Figure 2. SEM images of tungsten nanorods for different deposition times: (a) 10, (b) 20, (c) 30, (d) 60, (e) 90, and (f) 120 min.

2. EXPERIMENTAL SECTION

2.1. Schematic Overview. The various steps involved in the fabrication of highly ordered nano rods are shown in Figure 1a. First, the aluminum foil was subjected to an anodization process in order to generate alumina nanotubes. Next, the alumina nanotubes were chemically etched, resulting in highly ordered templates on the aluminum surface. These aluminum templates were then used as a substrate during the sputtering deposition process. The tilt was chosen such that the substrate normal and target normal form an angle of 85°. Subsequently, tungsten and aluminum were deposited separately using an RF-magnetron sputtering gun.

2.2. Aluminum Lattice Template. An aluminum sheet (99.99% pure) of 0.5 mm thick, obtained from Alfa Aesar, was annealed at 500 °C for 4 h. The annealed sheet of aluminum was then chemically cleaned and electro-polished to obtain a smooth, shining surface. The anodization was carried out in 0.3M/L oxalic acid solution at a constant cell potential of 40 V for one hour at 278 K. The anodized aluminum surface was subjected to chemical etching for 15 min in a mixture of phosphoric acid and chromic acid. The resulting aluminum lattice template (ALT) surface is shown in Figure 1b. The nominal RMS roughness of the obtained ALTs was 9.5 nm as measured by Atomic Force Microscope.

2.3. Glancing Angle RF Magnetron Sputtering. Tungsten (with 10% Ti) and Aluminum nanorods were grown on ALTs using glancing angle RF magnetron sputtering technique as previously mentioned and showed in Figure 1(a). The substrate-target distance was kept at 6 in. The nominal size of the substrate was 0.5" x 0.5". A base pressure of 5×10^{-7} Torr was achieved using a cryo pump. Ar gas was injected, through a gas injection ring just above the target, at a constant flow rate of 10 sccm to generate the plasma. The chamber pressure was kept at 1 mTorr during the deposition. Both the tungsten and aluminum nanorods were deposited at a power density of 5 W/cm^2 using 2 in. diameter targets. A DC stepper motor was used to rotate the ALT substrates at a constant rotation speed of 30 rpm. The deposition rate of tungsten and aluminum were 1.3 and 1.6 nm/min, respectively.

2.4. Surface Modification. Both the tungsten and aluminum nanorods have very high surface energy. A thin (5 nm) layer of TAF was coated on the nanorods using an effusion cell. TAF granules, obtained from Dupont, were placed in a quartz insert in a ceramic crucible. The quartz insert has a small orifice that allows a controlled evaporation of the polymers. The crucible was slowly heated using the heater coil in the effusion cell. 5 nm of TAF was coated at a deposition rate of 0.1 Å/s with a substrate rotation of 30 rpm. A quartz crystal monitor was used to measure the thickness of Teflon deposition.

2.5. Surface Morphology and Chemistry. The surface morphology of ALTs and nanorods grown on ALTs was characterized by Scanning Electron Microscope (JEOL 700) and Atomic Force Microscope (Veeco, Dimension 3100 Nanoscope III). The surface chemistry after the modification using TAF was studied using X-ray Photoelectron Spectroscopy (XPS). The XPS data were obtained on a Thermo Scientific K-Alpha X-ray photoelectron spectrometer at a background pressure of 1 x 10-9 Torr, using a monochromated Al Kα ($h\upsilon$ = 1436.6 eV) X-ray source. The x-ray beam used was 100 W, 400 μm in diameter. Survey scans (0−1350 eV) were taken on each sample at a pass energy (CAE) of 200 eV and 1 eV step size. The collected data were referenced to the C1s' peak to 284.6 eV. Narrow scans (25−40 eV width) of the peaks of interest (C1s, O1s, F1s, Ti2p, and W4f) were taken at a pass energy of 50 eV and 0.1 eV step size to provide higher resolution analysis of the peaks. Curve fitting was performed on the narrow scans using the Avantage V. 4.38 software.

2.6. Contact Angle Measurement. Teflon-coated tungsten and aluminum nanorods were characterized for their water repellency behavior using Kruss, USA contact angle measurement tool (EASY DROP DSA20E). A DI water droplet of 2 μL was dispensed on the surface using a computer-controlled automated syringe. The image of the water droplet was captured using a CCD camera. The static contact angle of the water drop was calculated using tangent method. The contact angle was measured on various positions of the sample, and an average value was reported.

3. RESULTS AND DISCUSSION

3.1. Fabrication of Tungsten and Aluminum Nanorods on ALT Substrates. All of the ALT substrates used for the nanorods' growth were identical in terms of the distance between seeds and surface roughness. The nominal dimension of the hexagonal seed structure was 100 nm, and the nominal roughness as measured by AFM was 9.5 nm. Tungsten and Aluminum nanorods were grown at different deposition times using glancing angle RF magnetron sputtering technique at 1 mTorr Ar pressure with a flow rate of 10 cc. Figure 2 shows the morphology of the tungsten nanorods grown on ALT substrates as a function of deposition time. As seen in Figure 2a, the preferential growth of the nanorods immediately started over the hexagonal lattice seed structures during the first 10 min of deposition. The growth of the nanorods on seed points continued further as the time of deposition increased to 20 min. Figure 2c clearly shows self-organized tungsten nanorods formed over the hexagonal lattice seeds. The preferential growth over lattice seeds is very much evident since it shows a hexagonal gap (HG) between the nanorods. After 60 min of deposition, tungsten nanorods started

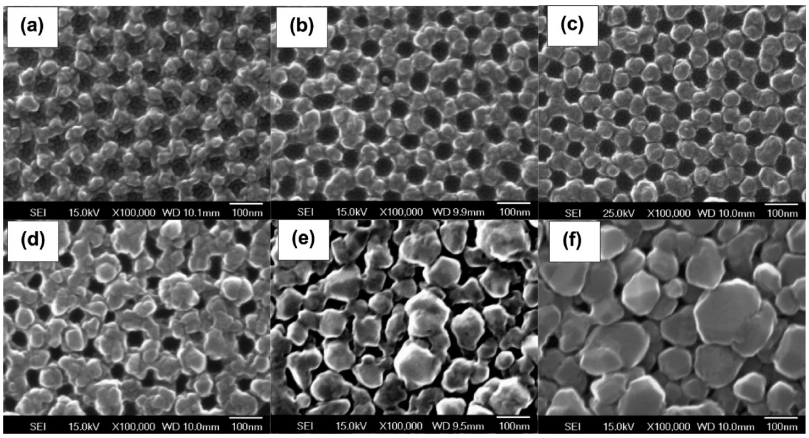

Figure 3. SEM images of aluminum nanorods for different deposition times: (a) 10, (b) 20, (c) 30, (d) 60, (e) 90, and (f) 120 min.

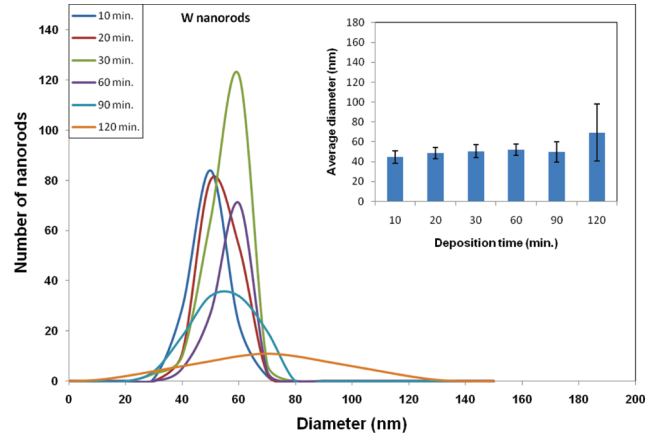

(a)

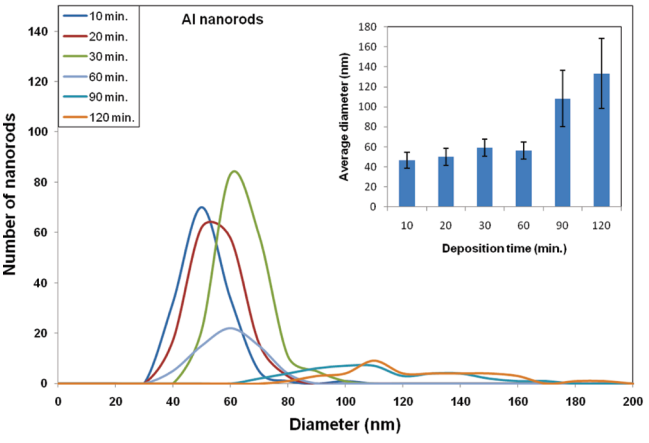

(b)

Figure 4. Size distribution curves and the variation of average diameter as a function of deposition times (inset), (a) for tungsten nanorods and (b) for aluminum nanorods.

presenting non-flat top surfaces, with mostly a top pyramidal geometry. Such pyramidal structures became even more prominent as the time of deposition increased to 90 min and further to 120 min. Such a unique tip geometry is known to occur for tungsten nanorods, making these materials excellent candidates for applications ranging from field emission to electromagnetic field enhancement especially[44,45] if a considerable degree of control over the long range assembly and dimensions of these structures is achieved. Similarly, the growth of aluminum nanorods on ALT substrates at various deposition times is shown in Figure 3. A similar trend of growth was observed for lower deposition times as in the case of tungsten. As the time of deposition increases to ~60 min, the nanorods tend to coalesce as seen in Figure 3c. The coalescence of nanorods becomes more dominant for deposition times of 90 and 120 mins. For these samples, the distribution of nanorods was random, and the long-range order disappeared.

The size distribution curves for the nanorods grown at various deposition times as obtained by a MATLAB image analysis code[22] are presented in Figure 4. For the size calculation, all of the nanorods were approximated into circles covering the nanorods. Figure 4a shows the size distribution curves for the W nanorods. It was found that, at lower deposition times, the curves have a Gaussian distribution with relatively narrow widths. The distribution profiles became wider with an increase in the deposition time, while the peaks shifted toward larger values indicating an increase in the nanorods' size with increasing time of deposition. The inset in Figure 4a shows the variation of average diameter of nanorods as a function of deposition time, which was found to remain relatively constant in the range of 40-50 nm, for deposition times of up to 90 min. The average diameter increases dramatically for the deposition time of 120 min reaching 70–80 nm. Similarly, the Al nanorods showed a relatively constant average diameter in the range 50-60 nm for deposition times of up to 60 min as seen in the inset of Figure 4b. As the deposition time increases above 60 min, the average diameter increases significantly and reaches almost 130 nm at the deposition time of 120 min. The distribution curves corresponding to the Al nanorods were much wider compared to the corresponding ones for the tungsten nanorods at all deposition times.

To confirm the obtained structures on the nanoseeds are nanorods, we have carried out side-view SEM analysis of tungsten films deposited for 90 min. As the substrates used in this study were aluminum, it was very difficult to get a side view by cleaving the substrate. Hence, we employed a scratch-and-tilt technique to characterize the side view of the nanorods. In this process, scratches were made on the top surfaces of the samples by using a sharp needle and SEM analysis was further used to image the cross-section by tilting the samples with 5°. Here, we present only a typical SEM side view of the tungsten nanorods

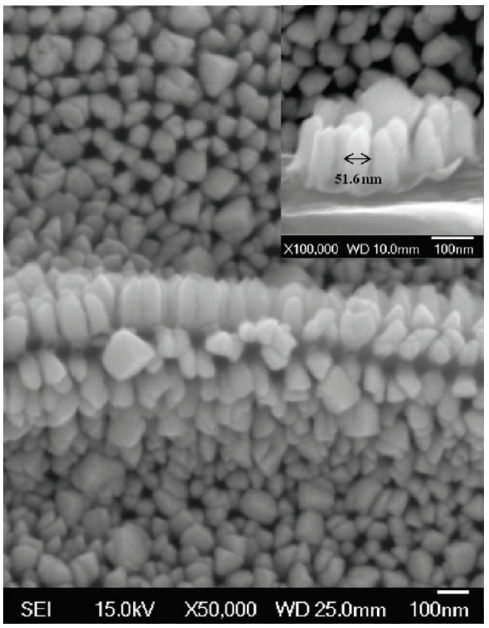

Figure 5. Typical SEM image of cross-sectional view of tungsten nanorods (90 min deposition) obtained by scratching the substrate. The image was taken by tilting the sample with 5°. The nanorods came out of the substrate at the scratched area provides the side view of nanorods. The inset shows side-view of the nanorods at a higher magnification.

deposited for 90 minutes in Figure 5. As shown and confirmed by the SEM analysis, the films grown by our process are composed of nanorods that are well separated and have uniform diameter morphologies over the entire height. The diameter calculated from the side view was found to be ~51.6 nm and is in good agreement with the diameter of the nanorods (average 49.82 nm) as determined by the Matlab image analysis approach (as shown in the bar diagram in Figure 4a).

In the traditional GLAD technique, the incoming flux has two components, lateral and vertical. As seen in Figure 5, for the incoming flux, the vector **F**, is given by[46]

$$F = F_{\text{vertical}} + F_{\text{lateral}} = F\cos\theta + F\sin\theta \qquad (1)$$

As both components of vapor flux deposit on the substrates, random islands form at the beginning of the deposition process. The adatom movement due to thermal diffusion on substrates is responsible for nucleation growth and hence increases the size of the islands. During deposition, the random islands act as shadowing centers and hence control the growth and the corresponding heights of the islands with the taller islands receiving more flux than the shorter ones. This competition continues during the entire deposition process and selective nanorods grow taller than the rest. The diameters of the nanorods increase in a direct relationship with their heights and depend on the ratio (ρ) of the deposition rate (r)/rotation speed (w).[23] Hence, on the flat surface, the nanostructures present non-cylindrical shapes, and the radius R is proportional with h^p where h is the height of the nanorods and p is the growth exponent. Previously, Karabacak et al.[47] have studied in detail the relationship between the height of the nanorods and the growth exponent. On the other hand, on the prepatterned substrate, the seeds provide the shadowing centers, as shown in Figure 6, and, in the beginning prior to the

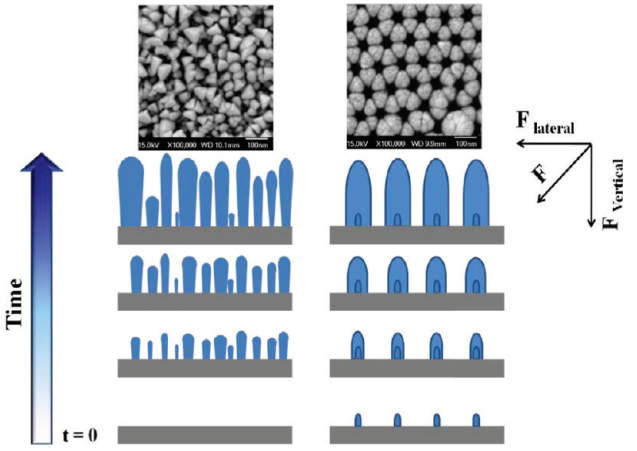

Figure 6. Schematic of GLAD on flat glass and ALT substrates.

radius saturation, induce similar growth rates as in the case of the non-seeded substrates. Once the radius saturates, it maintains the same value throughout the nanorod growth process. The effect of various seed geometries on the radius of nanostructures has been reported recently.[23] In order for the preferential growth to take place over the pre-patterned seeds, the seed geometry has to satisfy the following rule, determined by Jensen and Brett[48]

$$\Delta \leq h\tan a + d \qquad (2)$$

where Δ is center-to-center seed spacing, h is the height of the seeds, and d is the width of the seed. In the present case, the nominal height, h of the seeds is 9.5 nm, and the nominal width, d of the seeds is 13.5 nm (as obtained from SEM analysis, Figure 1b), and the angle of deposition was maintained at α = 85°. Hence, from eq 2, Δ required for preferential shadowing is ~122 nm. The ALT substrates used in the present case have hexagonally arranged arrays of seeds with a hexagon side length of 60 nm; the nominal distance between the sides is about 100 nm. Hence, the electrochemically obtained hexagonal seed geometry induces significant shadowing that prevents metal deposition between the seeds. As a result, it is expected that the growth of nanorods would be uniform and that no columnar broadening could occur with increasing thickness.

However, the growth of both tungsten and aluminum nanorods, as seen in Figures 2 and 3, shows a small amount of condensation between the seed structures especially during the first stage in the deposition process. Nevertheless, the predominant deposition took place over the seeds. This observation can be observed mainly because the lattice seeds do not have perfectly vertical sidewalls. A small percentage of atoms initially reach the spaces between the seeds, but, as the deposition time increases and the nanorods increase in height, this process ceases. To prevent between-seeds deposition, the sidewalls of the seeds need to be greater than 60°.[48] However, in the present case, the side wall angle was much lower than 60° (see AFM picture in the inset of Figure 1b). In addition, the materials were deposited using the sputtering technique at 1 mTorr, and the scattering of the oncoming flux is much higher at this pressure than for very high vacuum conditions on the order of 1×10^{-7} Torr. The scattering process reduces the mean free path of the atoms and facilitates some out-of-sight deposition. For tungsten, there was not much column broadening up to 90 min deposition time, with the average diameter of the nanorods in the range of 40−60 nm.

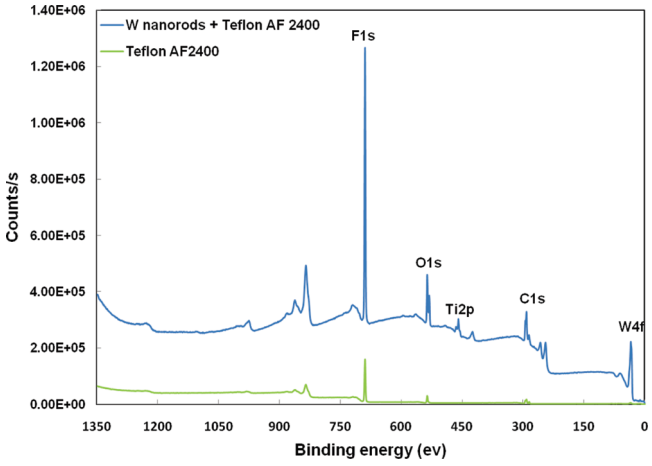

Figure 7. XPS spectra of TAF coated Tungsten nanorods.

However, for the deposition time of 120 min, a significant column broadening was observed with nanorods showing pyramidal geometry. The distribution of the nanorods becomes largely random with a wide diameter distribution as shown in Figure 4a. It is crucial to keep Δ intact in order to obtain an unaffected growth of the columnar structures. However, when the hexagonally arranged lattice seeds were used, the gap between the nanorods on the side of the hexagon started to decrease considerably due to the non-flat nanorod surface geometry observed to occur for deposition times of 60 min and higher. Hence, the condensation of metal atoms occurred everywhere except HG, and the resulting nanorods show significant broadening in the diameter and size distribution. However, for aluminum, the broadening of the nanorod columnar structure was observed much earlier—at 60 min deposition time—which can be explained primarily by the coalescence of the atoms. The coalescence of the atoms depends mainly on the diffusion process that is activated thermally and takes place after the initial condensation of the atoms on the substrate. The temperature of the substrate and melting point of the material play an important role in the surface diffusion. It has been suggested that thermally-activated surface diffusion normally occurs when the ratio of substrate temperature (T_s) over melting point of the deposition material is (T_m), $T_s/T_m \geq 0.24$.[12] Both the tungsten and aluminum were deposited at room temperature without an intentional heating; as a result, the temperature of the substrate (T_s) during the deposition remained below 330K in both the cases. Thus, for tungsten (T_m = 3695K), T_s/T_m was ~0.08, whereas for aluminum (T_m = 933 K), it was ~0.35. Hence, a significant coalescence was observed as expected for aluminum which increased with the deposition time resulting in almost continuous films at a deposition time of 120 min or higher. A reduction in substrate temperature to 223K that would reduce the $T_s/T_m \leq 0.24$ may prevent coalescence in the aluminum, and well-separated nanorods could be obtained even at higher deposition time.

3.2. Water Wettability of the Nanorods. As fabricated tungsten and aluminum nanorods have a very high surface energy. The water droplets dispensed on the as-fabricated nanorods were found to spread instantly, indicating a super hydrophilic behavior. To reduce the surface energy, both the tungsten and aluminum nanorods' surfaces were subsequently coated with 5 nm of TAF by thermal evaporation. The chemical structure of the TAF thin layer was analyzed by X-ray Photoelectron Spectroscopy (XPS). Figure 7 shows a typical XPS analysis collected on a 400 micrometer area of Teflon-coated tungsten nanorods along with the XPS spectrum of the reference TAF granules obtained under the same scan conditions. Figure 6 shows the XPS spectrum corresponding to the polymer layer deposited on top of the W nanorods, with peaks corresponding to F, O, C, and W. The W peak presence can be explained by the low thickness of the Teflon film, allowing the collection of signal from the underlying W structure. Compared to the reference Teflon AF 2400, the C peak percentage matches well, but, some variation was observed for the F and O elements. The escape depth of photoelectrons produced by the -rays is less than 10 nm, dependent upon the element Z number. The range for a high Z number like W is probably 5−10 nm, therefore the observation of the W peak, even through the surface is coated with TFA, indicates the thickness of the TFA layer is less than 10 nm. The F peak height related to the elemental concentrations was found to slightly decrease compared to the reference sample, whereas O shows an increase in the elemental concentration. This is due to the presence of TiO_2 detected on the surface. The O peak can be observed as a doublet, corresponding to both the metallic bonding of the TiO_2 and the organic O bonding in the TAF. The XPS analysis indicate that the presence of the TAF layer of a very low thickness (5 nm) was deposited on top of the nanorods structures, which is expected to significantly reduce the overall surface energy of the samples with an impact on the overall hydrophobicity of the samples.

Water repelling behavior of materials is basically explained by two models, Wenzel and Cassie. The Wenzel model[49] deals with an increase in surface area due to the roughness of material, and the Cassie model[50] takes into consideration the solid fraction of materials that is available for the water droplets to rest on when the air is trapped between gaps in the rough surface under water. These two models have been extensively used in understanding the nature of water interactions with various materials that present different surface roughness geometries, surface textures.[51,52] The Wenzel equation states that the apparent contact angle θ^* and roughness factor r (the ratio of actual over apparent surface area) may be conveyed by an equation,

$$\cos\theta^* = r\cos\theta \quad (3)$$

The relationship between θ^* and solid fraction f_s of the solid on which the water droplet sits (the rest on the air in the gap) is given by

$$\cos\theta^* = f_s(\cos\theta + 1) - 1 \quad (4)$$

The wetting property of water on both tungsten and aluminum nanorods was studied by measuring the static contact angle of water using sessile drop technique. To analyze the observed contact angles on tungsten and aluminum nanorods, the nature of the water droplets' interactions with a 25 nm thick Teflon AF 2400 film deposited by thermal evaporation on a glass substrate was investigated. The static contact angle of water, as measured using sessile drop technique, was found to be 120°. The surface morphology of this film was measured using atomic force microscopy, and the roughness factor was found to be ~1.04. Hence, the contact angle of water measured on this sample can be considered as Young's contact angle for our nano texture geometry of the nanorods. The SEM images presented in Figures 2 and 3 show clear HG space between the metal nanorods; therefore, when a water droplet is dispensed on such surfaces, the more realistic scenario would be to assume that air is being trapped

under water between the surfaces of the nanorods. Hence, we use the Cassie model for the prediction of contact angles.

3.3. Solid Fraction Measurement. To predict the contact angle using the Cassie model, the surface solid fraction available for water to sit on must be determined. The solid fraction of the nanorods was measured using two methods, a mathematical model and image analysis technique.

Because all of the nanorods were grown in a hexagonal arrangement over the Al lattice, a mathematical model was generated taking into consideration the size and the space between the nanorods since the solid fraction depends on these parameters. The higher the space between the nanorods, the lower the solid fraction; on the other hand, the lower the diameter of the nanorods, the lower the solid fraction. Figure 7 shows a schematic of the physical hexagonal lattice model that emulates the arrangement of the nanorods as seen in the corresponding SEM analysis. A similar approach has been used for hexagonal geometry to calculate surface area previously.[53] For the simplicity of the mathematical model, all of the nanorods and the spaces were assumed to be circles. Moreover, the size distribution curves shown in Figure 4 were obtained by image analysis technique (Figures 2 and 3) with the same assumptions. The diameter of the space between nanorods is represented as D, and the diameter of the nanorods is represented as d. A unit hexagon used for the calculation of the solid fraction was represented by a blue solid hexagon. As seen in Figure 8, the unit hexagon comprises 6 nanorods for the central hexagon and 6 spaces (each contributing half D) surrounding the central hexagon, as well as the central space.

Hence, the solid fraction of the unit hexagon can be represented as

$$f_s = \frac{\text{total area of the unit hexagon} - \text{areas occupied by spaces in the unit hexagon}}{\text{total area of unit hexagon}}$$

$$f_s = 1 - \frac{\frac{6}{3}\pi(D/2)^2 + \pi(D/2)^2}{6\,\pi(d/2)^2 + \frac{6}{3}\pi(D/2)^2 + \pi(D/2)^2} \quad (5)$$

After simplification, the equation can be represented as

$$f_s = 1 - \frac{1}{1 + 2(d/D)^2} \quad (6)$$

Finally, the unit hexagon has a packing density of 0.9 when it is filled with circles. Hence, the solid fraction is

$$f_s = 0.9\left(1 - \frac{1}{1 + 2\left(\frac{d}{D}\right)^2}\right) \quad (7)$$

We have used the average diameter of nanorods d (shown in Figures 2 and 3) and average space D obtained from the image analysis technique as input for the eq 7.

Similarly, we have developed an additional image analysis technique to measure the solid fraction directly from SEM images. More details of this technique can be found in our earlier work.[41] Panels a and b in Figure 9 show the variation of the solid fraction as a function of the deposition time calculated both from the mathematical model and the image analysis technique. The predicted values for the solid fractions based on the mathematical model are in good agreement with the measured values from the

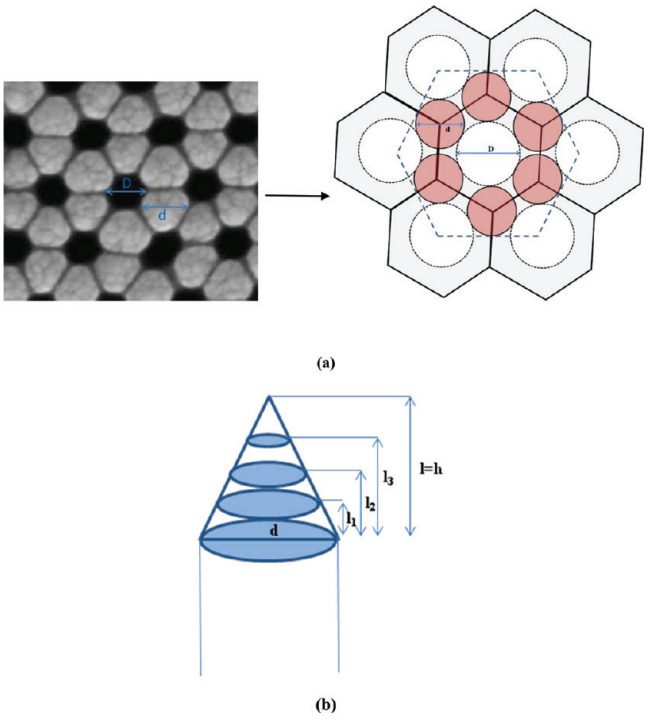

Figure 8. Schematic of mathematical model of (a) hexagon geometry with nanorods and spaces and (b) model of pyramidal geometry.

image analysis technique. Hence, we use the solid fraction obtained by image analysis technique for the further analysis of the contact angle results. The predicted and the observed contact angles along with the solid fractions of the nanorods are shown in Figure 10 as a function of the deposition time. For tungsten nanorods, as shown in Figure 9a, a slight increase in the contact angle was observed, from 147.1° to 150.1°, as the deposition time increased from 10 min to 20 min. A further increase in the deposition time induced a decrease in the contact angle to 141.6°. The contact angles began to increase again for higher deposition times and reached a fairly constant value of around 148°. For aluminum, the trend was precisely the opposite of that for tungsten as shown in Figure 9b. For higher deposition times, the measurement showed a steady decrease in contact angles, whereas at lower deposition times, the contact angles presented an upward trend.

The initial increase in contact angles for both tungsten and aluminum nanorods for higher solid fractions can be assigned to the increasing height of HG between nanorods. Although air can be trapped due to the shorter gaps, there is a possibility of water replacing air easily. The increase in the height of the nanorods at longer deposition times further increased the HG, which explains the higher measured values for the contact angles, opposite to the predicted decreasing contact angles, with increasing solid fraction. Further increase in the deposition time for aluminum resulted in a steady decrease in both the predicted and observed contact angles. This is largely due to the further increase in the solid fraction as shown in a and b in Figure 8. From eq 4, the increase in f_s, decreases Cassie angle for a given Young's contact angle. For tungsten, a further increase in deposition time showed no significant change in the predicted contact angles as the solid fraction remains almost the same. However, the observed contact angles showed a significant increase before leveling at around

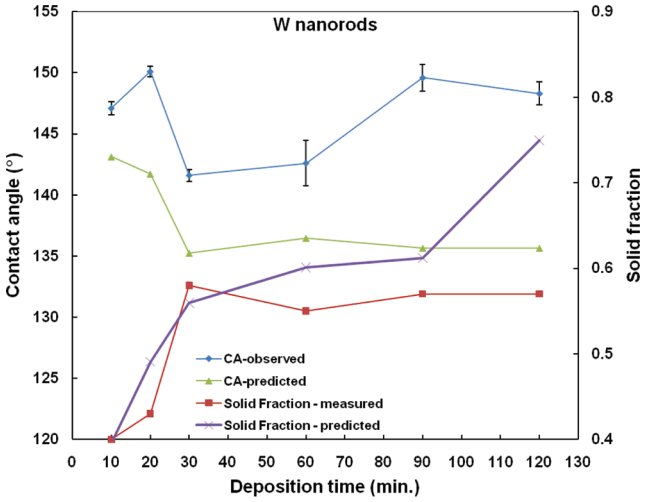

(a)

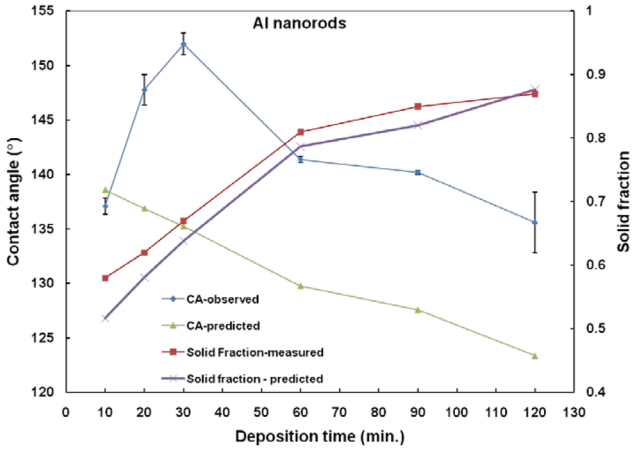

(b)

Figure 9. Variation in contact angles and solid fractions as a function of the deposition time: (a) for tungsten nanorods and (b) for aluminum nanorods.

148° for 120 min deposition time. This can be explained based on the surface morphology of the nanorods for the deposition time of 60 min and higher since they present pyramidal tips. Hence, the real solid fraction available for a water molecule to rest is much lower than the calculated solid fraction since the solid fraction was obtained by image analysis technique that captures only the base of pyramids rather than the actual tip of the pyramid. Similarly, our mathematical model in eq 5 basically assumes that the nanorods are circular objects and hence accounts only for the base of the nanorods deposited at 60 min and above. The effect of the pyramidal tips on water wetting behavior for the Ru and Pt nanorods has been previously studied by Lu et al.[42] In that study, the authors demonstrated that the hydrophilic behavior of the nanorods was controlled by the diameter and separation of the nanorods along with the pyramidal shape of the nanotips. Similarly, we have studied the effect of such a pyramidal geometry on the actual solid fraction in tungsten nanorods in detail elsewhere.[43] The approach to modifying the mathematical equation for the prediction of the solid fraction for a pyramidal geometry along with the modified equation is given below:

$$f_s = 0.9\left(1 - \frac{1}{1 + 2\left(\frac{d - \frac{2h}{\tan\alpha}}{D}\right)^2}\right) \quad (8)$$

where $h = (\sqrt{3})/(2)d$ as shown in Figure 7b; $\alpha = 0°$ represents a flat tip and $\alpha = 60°$ represents a perfect pyramidal tip. It is very important to note that the revised model is based on the assumption that the tungsten tips are perfectly pyramidal. As shown in Figure 7b, the height of the pyramid, represented as l, can vary from 0 to h. Hence, we can predict contact angles at various levels. Here we are presenting two extreme cases, $l = 0$ with flat tip and $l = 3/4h$, a near perfect pyramid. At $l = h$, it becomes a perfect pyramid and hence the solid fraction becomes zero. This case can be ruled out as the SEM images in Figure 2d−f show pyramids with different sizes of tips. With the modified solid fraction model, the solid fraction for 60 min deposited sample can vary from 0.6 (for l = 0) to 0.08 (for $l = 3/4h$). By replacing the f_s values calculated from eq 8 into eq 4, the predicted Cassie contact angle can vary between 136.4° (for $l = 0$) and 163.7° (for $l = 3/4h$). Hence, the value of the observed contact angle must fall in the range of 136.4−163.7°, depending on the level of l of the pyramidal tip. Since l is definitely not zero, as shown in Figure 2d−f, it can explain the significant increase in the contact angle for the tungsten nanorods deposited at 60 min and above.

CONCLUSIONS

We have successfully demonstrated the fabrication of self-organized metallic nanorods with a long range order by using a facile and scalable approach of nano-seed assisted GLAD technique. The results are consistent for two model metals, tungsten with a high melting point and aluminum with low melting point. However, the aluminum nanorods suffered significant coalescence due to severe surface diffusion that reduced the self-assembly and long range order with an increase in the deposition time. The growth mechanism was discussed based on the seed size and geometry along with the thermally activated surface diffusion. It is suggested that, by properly maintaining substrate temperature, such coalescence can be avoided to retain the long range order of self-organized nanorods. The results also suggest that, theoretically, by varying the size of anodic oxidized aluminum template, highly ordered hexagonal arrays of metallic nanostructures can be grown with sizes in the range of 20−400 nm. This approach to generating nanoseeds via anodic oxidization of aluminum/chemical etching has significant advantages over other methods of patterning in terms of simplicity, high throughput, and scalability. Both tungsten and aluminum nanorods, with a surface modification using TAF, showed water repellency behavior in the vicinity of superhydrophobicity. The results indicate that, by changing the size and distribution of the nanoseeds by varying anodization conditions, the hexagonal array of metallic nanorods can be grown on demand to suit a wide range of applications.

AUTHOR INFORMATION

Corresponding Author

*gkkannarpady@ualr.edu (G.K.K.); asbiris@ualr.edu (A.S.B.). Tel: 501-569-8067 (G.K.K.); 501-551-9067 (A.S.B.). Fax: 501-683-7601 (G.K.K.); 501-683-7601 (A.S.B.).

ACKNOWLEDGMENT

Financial support from U.S. Army (ERDC Cooperative Agreement Number: W912HZ-09-02-0008), Arkansas Science & Technology Authority (Grant # 08-CAT-03), Department of Energy (DE-FG36-06GO86072), and National Science Foundation (NSF/EPS-1003970) is greatly appreciated. The editorial assistance of Dr. Marinelle Ringer is also acknowledged.

REFERENCES

(1) Carsten, S.; A. Paul, A. *Nano Lett.* **2005**, *2*, 301–304.
(2) Shrawan, K. J.; Chao, P. L.; Zhen, H. C.; Kevin, J. C.; Igor, B.; Juan, A. Z.; Wenjun, Z.; Shuit, T. L. *J. Phys.Chem. C* **2010**, *17*, 7999–8004.
(3) Matthew, R.; Florencio, E. H.; Andres, D. C. *Anal. Chem.* **2006**, *2*, 445–451.
(4) Chang, W.; Ha, J. W.; Slaughter, L. S.; Link, S. *Proc. Natl. Acad. Sci. U.S.A.* **2010**, *7*, 2781–2786.
(5) Qunting, Q.; Peng, Z.; Bin, W.; Yuhui, C.; Shu, T.; Yuping, W.; Rudolf, H. *J. Phys. Chem. C* **2009**, *31*, 14020–14027.
(6) Wang, X.; Yang, B.; Zhang, H.; Feng, P. *Nanoscale Res. Lett.* **2007**, *8*, 405–409.
(7) Zhou, Q.; Liu, X.; Zhao, Y.; Jia, N.; Liu, L.; Yan, M.; Jiang, Z. *Chem. Commun.* **2005**, *39*, 4941–4942.
(8) Alouach, H.; Mankey, G. J. *Appl. Phys. Lett.* **2005**, *12*, 123114.
(9) Robbie, K.; Brett, M. J. *J. Vac. Sci. Technol., A* **1997**, *15*, 1460–1465.
(10) Xudong, W.; Xudong, W.; Christopher, J. S.; Zhong, L. W. *Nano Lett.* **2004**, *3*, 423–426.
(11) Limmer, S. J.; Seraji, S.; Wu, Y.; Chou, T. P.; Nguyen, C.; Cao, G. Z. *Adv. Funct. Mater.* **2002**, *1*, 59–64.
(12) Pavenayotin, N.; Stewart, J.,M.D.; Valles, J.; James, M.; Yin, A.; Xu, J. M. *Appl. Phys. Lett.* **2005**, *19*, 193111.
(13) Xia, Y.; Yang, P.; Sun, Y.; Wu, Y.; Mayers, B.; Gates, B.; Yin, Y.; Kim, F.; Yan, H. *Adv. Mater.* **2003**, *5*, 353–389.
(14) Chang, C. C.; Chang, C. S. *Solid State Commun.* **2005** *11-12*, 765–768.
(15) Zhixun, Luo; et al. *Nanotechnology* **2009**, *34*, 345601.
(16) Lv, R.; Cao, C.; Zhai, H.; Wang, D.; Liu, S.; Zhu, H. *Solid State Commun.* **2004**, *3-4*, 241–245.
(17) Schift, H.; Heyderman, L. J.; Auf der Maur, M.; Gobrecht, J. *Nanotechnology* **2001**, *2*, 173–177.
(18) Jaszewski, R. W.; Schift, H.; Schnyder, B.; Schneuwly, A.; Gröning, P. *Appl. Surf. Sci.* **1999**, *1-4*, 301–308.
(19) Robbie, K.; Brett, M. J.; Lakhtakia, A. *Nature* **1996**, *6610*, 616–616.
(20) Robbie, K.; Brett, M. J.; Lakhtakia, A. *J. Vac. Sci. Technol., A* **1995**, *6*, 2991–2993.
(21) Robbie, K.; Friedrich, L. J.; Dew, S. K.; Smy, T.; Brett, M. J. *J. Vac. Sci. Technol., A* **1995**, *3*, 1032–1035.
(22) Khedir, K. R.; Kannarpady, G. K.; Ishihara, H.; Woo, J.; Ryerson, C.; Biris, A. S. *Phys. Lett. A* **2010**, *43*, 4430–4437.
(23) Patzig, C.; Khare, C.; Fuhrmann, B.; Rauschenbach, B. *Phys. Status Solidi B* **2010**, *6*, 1322–1334.
(24) Hawkeye, M. M.; Brett, M. J. *J. Vac. Sci. Technol., A* **2007**, *5*, 1317–1335.
(25) Malac, M.; Egerton, R. F.; Brett, M. J.; Dick, B. *J. Vac. Sci. Technol., B* **1999**, *6*, 2671–2674.
(26) Dick, B.; Sit, J. C.; Brett, M. *J. Nano Lett.* **2001**, *2*, 71–73.
(27) Ye, D. -Y.; Karabacak, T.; Lim, B. K.; Wang, G. -W; Lu, T. -M. *Nanotechnology* **2004**, *7*, 817–821.
(28) Jensen, M. O.; Brett, M. J. *J. Nanosci. Nanotechnol.* **2005**, *5*, 723–728.
(29) Kesapragada, S. V.; Gall, D. *Appl. Phys. Lett.* **2006**, *20*, 203121.
(30) Zhao, Y.-P.; Ye, D.-X.; Wang, Pei-I.; Wang, G.-C.; Lu, T.-M. *Int. J. Nanosci.* **2002**, *1*, 87–97.
(31) Zhoua, C. M.; Gall, D. *Thin Solid Films* **2006**, *3*, 1223–1227.
(32) Traci, R. J.; Michelle, D. M.; Christy, L. H.; Richard, P. V. D. *J. Phys. Chem. B* **2000**, *45*, 10549–10556.
(33) Cheung, C. L.; Nikolić, R. J.; Reinhardt, C. E.; Wang, T. F. *Nanotechnology* **2006**, *5*, 1339.
(34) Christy, L. H.; Richard, P. V. D. *J. Phys. Chem. B* **2001**, *24*, 5599–5611.
(35) Yang, S. M.; Jang, S. G.; Choi, D. G.; Kim, S.; Yu, H.K. *Small* **2006**, *4*, 458–475.
(36) Feiyue, L.; Lan, Z.; Robert, M. M. *Chem. Mater.* **1998**, *9*, 2470–2480.
(37) Lee, W. *J. Miner. Met. Mater. Soc.* **2010**, *6*, 57–63.
(38) Lafuma, A.; Quere, D. *Nat. Mater.* **2003**, *7*, 457–60.
(39) Fan, J. -G.; Tang, X. -J.; Zhao, Y. -P. *Nanotechnology* **2004**, *15*, 501–504.
(40) Fan, J. -G.; Zhao, Y. -P. *Nanotechnology* **2008**, *19*, 155707–155713.
(41) Fan, J. -G.; Zhao, Y. -P. *Langmuir* **2010**, *11*, 8245–8250.
(42) Ye, D. -X.; Lu, T. -M.; Karabacak, T. *Phys. Rev. Lett.* **2008**, *100*, 256102.
(43) Khedir, R. K.; Ganesh, K. K.; Hidetaka, I.; Justin, W.; Alexandru, S. B. *Langmuir* **2011**, 4661–4668.
(44) Singh, J. P.; Karabacak, T.; Lu, T. -M.; Wang, G. -C.; Koratkar, N. *Appl. Phys. Lett.* **2004**, *15*, 3226–3228.
(45) Gillich, D. J.; Teki, R.; Fullem, T. Z.; Kovanen, A.; Blain, E.; Chrisey, D. B.; Lu, T.; Danon, Y. *Nano Today* **2009**, *3*, 227–234.
(46) Dick, B.; Brett, M. J.; Smy, T. *J. Vac. Sci. Technol., B* **2003**, *6*, 2569–2575.
(47) Karabacak, T.; Singh, J. P.; Zhao, Y. -P.; Wang, G. -C.; Lu, T. -M. *Phys. Rev. B* **2003**, 125408.
(48) Jensen, M. O.; Brett, M. J. *IEEE Trans. Nanotechnol.* **2005**, *2*, 269–277.
(49) Wenzel, R. N. *Ind. Eng. Chem.* **1936**, *8*, 988–994.
(50) CASSIE, A. B. D.; BAXTER, S. *Trans. Farady Soc.* **1944**, 546–551.
(51) Bico, J.; Thiele, U.; Quéré, D. *Colloids Surf. Physicochem. Eng. Aspects* **2002**, *1-3*, 41–46.
(52) Kannarpady, G. K.; Sharma, R.; Liu, B.; Trigwell, S.; Ryerson, C.; Biris, A. S. *Appl. Surf. Sci.* **2010**, *6*, 1679–1682.
(53) Shankar, K.; Mor, G. K.; Prakasam, H. E.; Yoriya, S.; Paulose, M.; Varghese, O. K.; Grimes, C. A. *Nanotechnology* **2007**, *6*, 065707.